

# Numerical Implementation of Imperfect Interfaces

John A. Nairn

*Wood Science & Engineering, Oregon State University, Corvallis, OR, 97331, USA*

---

## Abstract

One approach to characterizing interfacial stiffness is to introduce imperfect interfaces that allow displacement discontinuities whose magnitudes depend on interfacial traction and on properties of the interface or interphase region. This work implemented such imperfect interfaces into both finite element analysis and the material point method. The finite element approach defined imperfect interface elements that are compatible with static, linear finite element analysis. The material point method interfaces extended prior contact methods to include interfaces with arbitrary traction-displacement laws. The numerical methods were validated by comparison to new or existing stress transfer models for composites with imperfect interfaces. Some possible experiments for measuring the imperfect interface parameters needed for modeling are discussed.

*Keywords:* Imperfect Interfaces, Material Point Method, Finite Element Analysis, Wood-Based Composites

---

## 1. Introduction

An interface between phases in a composite has at least two distinct properties — strength and stiffness. “Strength” is used here as a generic term for interfacial damage or failure. Interfacial strength properties are important when considering composite failure properties. “Stiffness” is used here as a generic term for stress transfer between components of a composite. Interfacial stiffness properties are important when considering composite mechanical properties. Prior to interfacial damage, the role of the interface is solely characterized by its stiffness properties while its strength properties are irrelevant. This paper is on numerical modeling of those interfacial stiffness properties and uses the concept of an “imperfect” interface to lump complexities of a three dimensional interphase zone into a two dimensional interface model.

This work was motivated by wood-based composites such as oriented strand board, plywood, laminated veneer lumber, glue-lam, fiber board, and particle board [1]. These wood products are made with a minimal amount of glue and have complicated glue lines. Various effects influence glue line properties such as species of wood, surface preparation, glue penetration into wood cells, and moisture content of the wood. Numerous test standards for characterizing wood glue lines are available, but nearly all focus on interfacial strength or toughness. Because most wood structure design is stiffness driven, modeling methods and experiments that characterize the role of interfacial stiffness properties on the stiffness of wood-based composites are also needed.

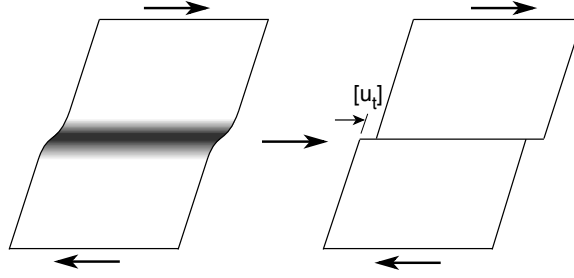


Figure 1: Schematic view for replacement of a 3D interphase (left) by a 2D interface with a displacement discontinuity (right).

Glue line interfaces in wood (and many other interfaces) are complex three dimensional structures with a transition in properties between two bonded materials. Modeling such structures is difficult and depends on many unknown, and possibly unknowable, properties. One modeling method is to replace the 3D structure by a 2D interface and to reduce the unknown properties to a few measurable “interface parameters.” The goal is to develop a 2D interface model that sufficiently describes stress transfer across the real 3D interface. The principle is illustrated in Fig. 1. The left side shows an interphase zone with a gradient in properties between two materials and complex shear deformations. The right side shows a simplified composite where macroscopic deformations are the same, but a 2D interface has replaced the interphase zone. Deformation of the interphase is modeled by allowing a displacement discontinuity at the 2D interface. The displacement discontinuity magnitude should be a function of the traction vector in the direction of the discontinuity and stiffness properties of the imperfect interface [2, 3, 4, 5] .

For a general 2D interface between 3D materials, the traction vector can be divided into components normal to the interface,  $T_n$ , and parallel to the interface,  $T_t$ . Prior analytical models [2, 3, 4] use the simplest assumption where traction is proportional to displacement discontinuity

$$T_n = D_n[u_n] \quad \text{and} \quad T_t = D_t[u_t] \quad (1)$$

where  $[u_n]$  and  $[u_t]$  are the normal and tangential displacement discontinuities, and  $D_n$  and  $D_t$  are the interface parameters. These parameters reduce all properties of the 3D interphase to two interface stiffness properties. As  $D_n$  and  $D_t$  approach zero, tractions approach zero and the interface is debonded. As  $D_n$  and  $D_t$  approach infinity, displacement discontinuities approach zero and the interface is perfect. All other values describe an imperfect interface to model the response of a interphase. The example interface is linear. The approach can extend to non-linear models by introducing non-linear relations between traction and displacement discontinuity.

Modeling with imperfect interfaces requires two tasks. The first is to model arbitrary composites with imperfect interfaces. Some analytical models are available for ideal geometries and linear interfaces [2, 4]. Numerical models are needed for complex geometries and non-linear interfaces. This paper describes implementation of imperfect interfaces into finite element analysis (FEA) and into the material point method (MPM). The implementations were

verified by comparison to new or existing analytical models of composites with imperfect interfaces. The FEA implementation was limited to linear interfaces and quasi-static calculations. The MPM implementation extended previous work on contact between materials [6] and included non-linear interfaces.

The second task for modeling with imperfect interfaces is to propose methods for measuring interface parameters such as  $D_n$  and  $D_t$ . This paper includes some observations about experimental approaches to measuring those stiffness properties.

## 2. Numerical Implementation of Imperfect Interfaces

### 2.1. Finite Element Analysis

The finite element analysis (FEA) implementation used a linear interface traction law since the goal was to derive an efficient element for static FEA of composites. The potential energy associated with an imperfect interface is [3]

$$\phi_i = \frac{1}{2} \int_{S_i} \vec{T} \cdot [\vec{u}] dS \quad (2)$$

where  $S_i$  is the interfacial area,  $\vec{T}$  is the traction, and  $[\vec{u}] = \vec{u}^{(1)} - \vec{u}^{(2)}$  is the interfacial displacement discontinuity (superscripts indicate side of the interface). For a planar 2D problem with an interface following the traction-displacement law in Eq. (1), the displacement discontinuity and traction vectors can be written in component form as

$$[\vec{u}] = [u_n] \hat{n}_1 + [u_t] \hat{t}_1 \quad \text{and} \quad \vec{T} = D_n [u_n] \hat{n}_1 + D_t [u_t] \hat{t}_1 \quad (3)$$

where  $\hat{n}_1$  and  $\hat{t}_1$  are unit normal vectors directed as shown for FEA in Fig. 2 along side 1. The potential energy is a line integral along the interfacial path,  $L_i$ :

$$\phi_i = \frac{t}{2} \int_{L_i} (D_n [u_n]^2 + D_t [u_t]^2) dl = \frac{t}{2} \int_{L_i} [\mathbf{u}]^T \{\mathbf{D}\} [\mathbf{u}] dl \quad (4)$$

where  $t$  is thickness,

$$[\mathbf{u}] = ([u_n], [u_t]) \quad \text{and} \quad \{\mathbf{D}\} = \begin{pmatrix} D_n & 0 \\ 0 & D_t \end{pmatrix} \quad (5)$$

Extension to axisymmetric problems is given below; extension to 3D problems requires the tangential direction to be in the tangential direction of the displacement discontinuity vector and integration over the entire interfacial surface.

The normal and tangential interface displacement differences can be expressed in terms surface displacements and derivatives along the interfacial path:

$$[u_n] = [\vec{u}] \cdot \hat{n}_1 = [\vec{u}] \cdot \left( \frac{dy}{dl}, -\frac{dx}{dl} \right) \quad \text{and} \quad [u_t] = [\vec{u}] \cdot \hat{t}_1 = [\vec{u}] \cdot \left( \frac{dx}{dl}, \frac{dy}{dl} \right) \quad (6)$$

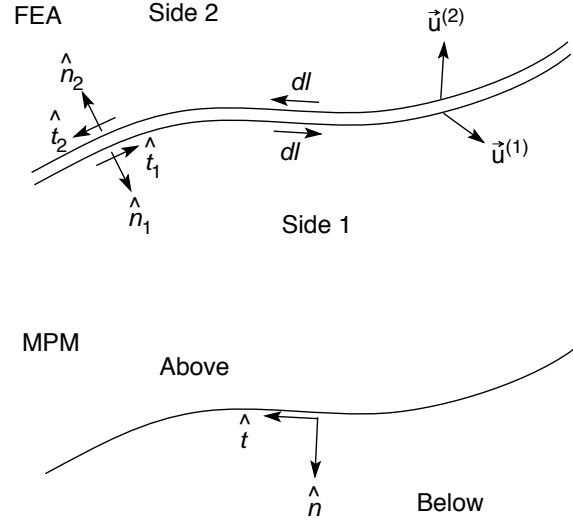


Figure 2: Arbitrary interfaces for analysis by FEA or MPM. The FEA interface shows definition of the two sides and the various normal vectors. The MPM interface shows definition of normal vectors and the meaning of “above” and “below” the crack.

which follows because  $\hat{n}_1 = (dy/dl, -dx/dl) = -\hat{n}_2$  and  $\hat{t}_1 = (dx/dl, dy/dl) = -\hat{t}_2$ . The energy becomes

$$\phi_i = \frac{t}{2} \int_{S_i} [\vec{u}]^T \begin{pmatrix} D_n \left(\frac{dy}{dl}\right)^2 + D_t \left(\frac{dx}{dl}\right)^2 & (D_t - D_n) \frac{dx}{dl} \frac{dy}{dl} \\ (D_t - D_n) \frac{dx}{dl} \frac{dy}{dl} & D_n \left(\frac{dx}{dl}\right)^2 + D_t \left(\frac{dy}{dl}\right)^2 \end{pmatrix} [\vec{u}] dl \quad (7)$$

Next, subdivide the interface into elements each with  $2n$  nodes and each with the undeformed state having the two sides in contact (see Fig. 3A). In other words, node  $i$  has the same initial position as node  $2n+1-i$ . Because the two sides are initially coincident,  $n$  shape functions ( $N_i(\xi)$  in element coordinate  $\xi$ ), are sufficient. The expanded surface displacements are

$$\vec{u}^{(1)} = \sum_{i=1}^n N_i(\xi) (u_i, v_i) \quad \text{and} \quad \vec{u}^{(2)} = \sum_{i=1}^n N_i(\xi) (u_{2n+1-i}, v_{2n+1-i}) \quad (8)$$

where  $u_i$  and  $v_i$  are nodal  $x$ - and  $y$ -direction displacements. The displacement difference becomes

$$[\vec{u}] = \begin{pmatrix} N_1(\xi) & 0 & N_2(\xi) & 0 & \cdots & N_{2n}(\xi) & 0 \\ 0 & N_1(\xi) & 0 & N_2(\xi) & \cdots & 0 & N_{2n}(\xi) \end{pmatrix} \begin{Bmatrix} u_1 \\ v_1 \\ \vdots \\ u_{2n} \\ v_{2n} \end{Bmatrix} \quad (9)$$

where, for convenience, shape functions are extended to nodes  $n+1$  to  $2n$  using

$$N_i(\xi) = -N_{2n+1-i}(\xi) \quad \text{for} \quad i = n+1, \dots, 2n \quad (10)$$

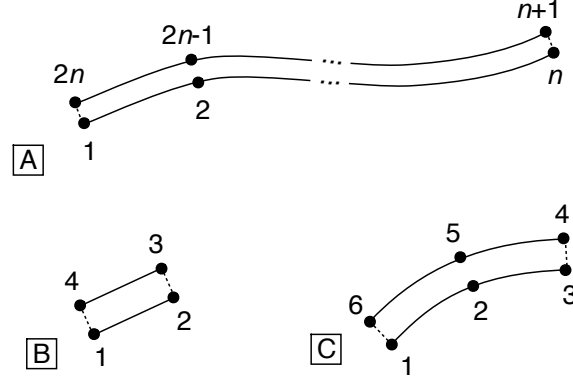


Figure 3: Imperfect interface element for FEA. A. Arbitrary element with  $2n$  nodes. B. A linear, 4-noded element. C. A quadratic, 6-noded element.

such that surface 2 displacements are expressed as

$$\vec{u}^{(2)} = - \sum_{i=n+1}^{2n} N_i(\xi)(u_i, v_i) \quad (11)$$

To evaluate the unit normal vectors (*i.e.*,  $dx/dl$  and  $dy/dl$ ), the  $x$  and  $y$  coordinates along the interface are expanded in the same  $n$  shape functions

$$x(\xi) = \sum_{i=1}^n N_i(\xi)x_i \quad \text{and} \quad y(\xi) = \sum_{i=1}^n N_i(\xi)y_i \quad (12)$$

where  $(x_i, y_i)$  are the coordinates of node  $i$ . The expansion is similar to isoparametric elements except here  $2n$  shape functions are needed to expand displacements on both surfaces while only  $n$  shape functions are needed for the coordinates. The derivatives in terms of shape functions are:

$$\frac{dx}{dl} = \frac{x'(\xi)}{\frac{dl}{d\xi}} = \frac{\sum_{i=1}^n N'_i(\xi)x_i}{\frac{dl}{d\xi}} \quad \text{and} \quad \frac{dy}{dl} = \frac{y'(\xi)}{\frac{dl}{d\xi}} = \frac{\sum_{i=1}^n N'_i(\xi)y_i}{\frac{dl}{d\xi}} \quad (13)$$

where the arc-length derivative is

$$\frac{dl}{d\xi} = \sqrt{x'(\xi)^2 + y'(\xi)^2} \quad (14)$$

Finally, substituting  $[\vec{u}]$ ,  $dx/dl$ , and  $dy/dl$  into Eq. (7), the interfacial potential energy in the element becomes

$$\phi_i = \frac{1}{2} \{\mathbf{u}\}^T \{\mathbf{K}_I\} \{\mathbf{u}\} \quad (15)$$

where  $\{\mathbf{u}\}$  is the vector of nodal displacements (see Eq. (9)) and  $\{\mathbf{K}_I\}$  is the interfacial stiffness matrix. Explicit expressions for the elements of this  $2n \times 2n$  matrix are

$$\{\mathbf{K}_I\}_{ij} = t \int_{-1}^1 N_{\frac{i+1}{2}} N_{\frac{j+1}{2}} \frac{D_t x'(\xi)^2 + D_n y'(\xi)^2}{\sqrt{x'(\xi)^2 + y'(\xi)^2}} d\xi \quad \text{for } i, j \text{ odd} \quad (16)$$

$$\{\mathbf{K}_I\}_{ij} = t \int_{-1}^1 N_{\frac{i}{2}} N_{\frac{j}{2}} \frac{D_n x'(\xi)^2 + D_t y'(\xi)^2}{\sqrt{x'(\xi)^2 + y'(\xi)^2}} d\xi \quad \text{for } i, j \text{ even} \quad (17)$$

$$\{\mathbf{K}_I\}_{ij} = t \int_{-1}^1 N_{\frac{i+1}{2}} N_{\frac{j}{2}} \frac{(D_t - D_n) x'(\xi) y'(\xi)}{\sqrt{x'(\xi)^2 + y'(\xi)^2}} d\xi \quad \text{for } i \text{ odd, } j \text{ even} \quad (18)$$

$$\{\mathbf{K}_I\}_{ij} = t \int_{-1}^1 N_{\frac{i}{2}} N_{\frac{j+1}{2}} \frac{(D_t - D_n) x'(\xi) y'(\xi)}{\sqrt{x'(\xi)^2 + y'(\xi)^2}} d\xi \quad \text{for } i \text{ even, } j \text{ odd} \quad (19)$$

This element can be incorporated into standard FEA code including potential energy calculations associated with the interface. The above stiffness matrix is for planar analyses. To extend to a stiffness matrix (per radian) for axisymmetric analyses, replace the thickness  $t$  by  $r(\xi)$  in the integrand for the radial location at dimensionless position  $\xi$ .

## 2.2. Specific Elements

Selecting  $n = 2$  gives a 4-node linear interface element (see Fig. 3B). The shape functions are

$$N_1(\xi) = \frac{1-\xi}{2}, \quad N_2 = \frac{1+\xi}{2}, \quad N_3(\xi) = -N_2(\xi), \quad N_4(\xi) = -N_1(\xi) \quad (20)$$

where  $\xi$  extends from  $-1$  to  $1$ , resulting in

$$x'(\xi) = \frac{\Delta x}{2}, \quad y'(\xi) = \frac{\Delta y}{2}, \quad \text{and} \quad \frac{dl}{d\xi} = \frac{\Delta l}{2} \quad (21)$$

where  $\Delta x = x_2 - x_1$ ,  $\Delta y = y_2 - y_1$ , and  $\Delta l$  is the element length. For this element, the stiffness matrix can be exactly integrated. For example, the first row of the stiffness matrix is

$$\{\mathbf{K}_I\}_{11} = -\{\mathbf{K}_I\}_{17} = \frac{t}{3\Delta l} (D_t (\Delta x)^2 + D_n (\Delta y)^2) \quad (22)$$

$$\{\mathbf{K}_I\}_{12} = -\{\mathbf{K}_I\}_{18} = \frac{t \Delta x \Delta y}{3\Delta l} (D_t - D_n) \quad (23)$$

$$\{\mathbf{K}_I\}_{13} = -\{\mathbf{K}_I\}_{15} = \frac{t}{6\Delta l} (D_t (\Delta x)^2 + D_n (\Delta y)^2) \quad (24)$$

$$\{\mathbf{K}_I\}_{14} = -\{\mathbf{K}_I\}_{16} = \frac{t \Delta x \Delta y}{6\Delta l} (D_t - D_n) \quad (25)$$

The matrix can also be integrated numerically using two-point Gaussian quadrature (this numerical result is exact for linear elements). An advantage of numerical integration is that it generalizes better with the quadratic element described next that can not be exactly integrated.

Selecting  $n = 3$  gives a 6-node quadratic interface element (see Fig. 3C). The shape functions are

$$N_1(\xi) = -\frac{\xi(1-\xi)}{2}, \quad N_2 = 1 - \xi^2, \quad N_3 = \frac{\xi(1+\xi)}{2}, \quad (26)$$

$$N_4(\xi) = -N_3(\xi), \quad N_5(\xi) = -N_2(\xi), \quad \text{and} \quad N_6(\xi) = -N_1(\xi) \quad (27)$$

resulting in

$$x'(\xi) = \frac{\Delta x}{2} + \Delta m_x \xi, \quad y'(\xi) = \frac{\Delta y}{2} + \Delta m_y \xi \quad (28)$$

and

$$\frac{dl}{d\xi} = \sqrt{x'(\xi)^2 + y'(\xi)^2} \quad (29)$$

where  $\Delta x = x_3 - x_1$ ,  $\Delta y = y_3 - y_1$ ,  $\Delta m_x = x_1 + x_2 - 2x_3$ , and  $\Delta m_y = y_1 + y_3 - 2x_2$ . Because  $dl/d\xi$  depends on  $\xi$ , the stiffness matrix elements can no longer be exactly integrated. The calculations in this paper found the stiffness matrix using 4-point Gaussian quadrature.

### 2.3. Alternate Finite Element Methods

An alternative FEA method for interfaces is to connect two surfaces by a row of springs. But, a linear imperfect interface and a row of linear springs are fundamentally different. First, the resulting global stiffness matrices are different. By definition of a stiffness matrix, the element forces along an imperfect interface are

$$\{\mathbf{F}\} = \{\mathbf{K}_i\}\{\mathbf{u}\} \quad \text{where} \quad \{\mathbf{F}\} = \left( (F_x)_1, (F_y)_1, \dots, (F_x)_{2n}, (F_y)_{2n} \right) \quad (30)$$

and  $(F_x)_i$  and  $(F_y)_i$  are components of the interface element forces at node  $i$ . From the stiffness matrix for imperfect interfaces, the nodal forces depend on nodal displacements for all nodes in the interfacial element. In contrast, the forces in a row of springs depend only on the displacement difference between the two nodes connecting each spring. Second, imperfect interface elements were derived from rigorous variational mechanics of imperfect interfaces [3] and contribute to global energy. Thus energy results can be used for rigorous evaluation of imperfect interface effects on stiffness properties of a composite.

The imperfect interface elements could be expressed as a special case of cohesive zone elements. For example, early development of cohesive zone elements [7] begins with a potential energy function analogous to Eq. (2). But, cohesive zone elements always emphasize failure properties and thus their traction laws focus on maximum stress and shape of the traction-opening displacement law after failure. Standard cohesive zone elements require non-linear finite element analysis. In contrast, imperfect interface elements deal only with the initial slope of the traction-opening displacement law. Their use is restricted to the role of the interface in the stiffness properties of the composite, but they are efficient because they can be used in linear finite element analyses.

## 2.4. Material Point Method

The material point method (MPM) is a particle based method in which equations are solved on a background grid [8]. Algorithms for dealing with contact have been developed by allowing multiple velocity fields on the background grid. Previous work models slip, stick, or frictional sliding at material interfaces [6, 9] or on crack surfaces [10, 11, 12]. The multiple velocity fields are for different materials or for two sides of a crack, respectively. This section describes extension of MPM contact methods to include interface traction laws.

The key tasks in MPM with contact methods for slip, stick, or frictional sliding are these:

1. Extrapolate particle data to the nodes calculating, among other quantities,  $\vec{v}_{i,1}^\alpha$  and  $m_i^\alpha$  or the velocity and mass on node  $i$  associated with velocity field  $\alpha$ . For contact, each material is associated with its' own velocity field.
2. Nodes with multiple velocity fields are potentially nodes in contact. First, the initially-extrapolated velocities on such nodes are stored as  $\vec{v}_{i,0}^\alpha$ . Second, the nodal values are examined to determine if the two velocity fields are in contact. If there is contact, the nodal velocities are altered to [6, 9]

$$\vec{v}_{i,2}^\alpha = \vec{v}_{i,1}^\alpha + \Delta\vec{v}_i^\alpha \quad (31)$$

where the change in each velocity field is

$$\Delta\vec{v}_i^\alpha = -\Delta v_{i,n}^\alpha \hat{n}^\alpha - \min(\mu\Delta v_{i,n}^\alpha, \Delta v_{i,t}^\alpha) \hat{t}^\alpha \quad (32)$$

Here  $\mu$  is the coefficient of friction and  $\Delta v_{i,n}^\alpha$  and  $\Delta v_{i,t}^\alpha$  are components of the difference between velocity field  $\alpha$  and the center-of-mass velocity in the normal and tangential directions:

$$\Delta v_{i,n}^\alpha = (\vec{v}_{i,1}^\alpha - \vec{v}_i^{cm}) \cdot \hat{n}^\alpha \quad \text{and} \quad \Delta v_{i,t}^\alpha = (\vec{v}_{i,1}^\alpha - \vec{v}_i^{cm}) \cdot \hat{t}^\alpha \quad (33)$$

where  $\hat{n}^\alpha$  and  $\hat{t}^\alpha$  are unit vectors in the normal and tangential directions of sliding. A change in velocity can be associated with a contact force  $\vec{f}_i^\alpha = m_i^\alpha \Delta\vec{v}_i^\alpha / \Delta t$ , where  $\Delta t$  is the time step. Thus the two options in  $\min()$  correspond to frictional sliding or stick conditions. During frictional sliding the normal and tangential components of  $\vec{f}_i^\alpha$  are related by  $f_{i,t}^\alpha = \mu f_{i,n}^\alpha$ . During stick conditions all motion moves within the center-of-mass velocity field and the algorithm reverts to conventional, single-velocity-field MPM.

3. Once contact velocities are altered, the MPM algorithm proceeds as usual for each velocity field [9]. The standard tasks include computation of internal forces due to particle stress,  $\vec{f}_{i,int}^\alpha$ , computation of external forces,  $\vec{f}_{i,ext}^\alpha$ , computation of nodal accelerations,  $\vec{a}_i^\alpha = (\vec{f}_{i,int}^\alpha + \vec{f}_{i,ext}^\alpha) / m_i^\alpha$ , and updating of nodal velocities

$$\vec{v}_{i,3}^\alpha = \vec{v}_{i,2}^\alpha + \vec{a}_i^\alpha \Delta t \quad (34)$$

4. The updated velocity may induce new contact situations, thus the next step is to repeat contact calculations from step (ii) and alter nodal velocities if there is contact to

$$\vec{v}_{i,4}^\alpha = \vec{v}_{i,3}^\alpha + \Delta\vec{v}_i^\alpha \quad (35)$$

5. Finally, the MPM algorithm updates velocities and positions of all particles. If this update is done with the final velocities ( $\vec{v}_{i,4}^\alpha$ ) and the accelerations in step (iii), however, the update would be wrong. Before the update, it is therefore necessary to recalculate the nodal accelerations of contact nodes to correspond to the acceleration that changes the initially-extrapolated velocity in step (i) ( $\vec{v}_{i,0}^\alpha$ ) to the final velocity:

$$\vec{a}_i^\alpha = \frac{\vec{v}_{i,4}^\alpha - \vec{v}_{i,0}^\alpha}{\Delta t} \quad (36)$$

Once these *consistent* accelerations are found at contact nodes, the particle update proceeds by standard MPM methods.

Because imperfect interfaces are internal to an object and transmit stresses by a traction law, it makes physical sense to model them as contributing to internal forces analogous to forces arising from other internal stresses. This approach requires modification of step (iii). As an aside, one might also imagine an imperfect interface as part of contact calculations and therefore modifying steps (ii) and (iv). This approach was tried and gave reasonable results, but raised physical concerns regarding contact. It was abandoned without further study in favor of the internal force approach. The contact tasks were thus modified as follows:

1. When extrapolating velocity fields, also extrapolate the displacements of particles to the nodes leading to  $\vec{u}_i^\alpha$ .
2. When doing contact calculations, first determine if a node with multiple velocity fields is a contact interface or if it is an imperfect interface. If it is a contact interface, proceed as before. If it is an imperfect interface, then  $\Delta \vec{v}_i^\alpha = 0$ . All interfaces in these calculations were imperfect interfaces. Contact interfaces and imperfect interfaces may be mixed providing the correct nature of each multiple-velocity field node can be determined.
3. When calculating forces, return to all imperfect interface nodes and calculate normal and tangential tractions as:

$$T_n = D_n[u_n] \quad \text{and} \quad T_t = D_t[u_t] \quad (37)$$

where

$$[u_n] = -(\vec{u}_i^\alpha - \vec{u}_i^\beta) \cdot \hat{n} \quad \text{and} \quad [u_t] = -(\vec{u}_i^\alpha - \vec{u}_i^\beta) \cdot \hat{t} \quad (38)$$

where  $\alpha$  and  $\beta$  refer to velocity fields “above” and “below” the interface and the normal vectors,  $\hat{n}$  and  $\hat{t}$ , are directed *from* above *to* below as shown for MPM in Fig. 2. The additional internal forces applied above and below the crack are then

$$\Delta f_{i,int}^\alpha = (T_n \hat{n} + T_t \hat{t})A \quad \text{and} \quad \Delta f_{i,int}^\beta = -\Delta f_{i,int}^\alpha \quad (39)$$

where  $A$  is the surface area of the interface on the grid. For a regular, square, 2D grid,  $A = t\Delta x$  where  $t$  is thickness and  $\Delta x$  is length of the element sides. For non-square or irregular grid,  $A$  is the interfacial area associated with that node. The velocity update in this task proceeds as above, but now using the modified internal forces.

4. Repeat contact calculations for contact interface nodes with multiple velocity fields, but do no calculations for imperfect interface nodes.
5. Finally, modify nodal accelerations if needed, but these modifications are only needed for contact interface nodes and not for imperfect interface nodes.

In contrast to the linear FEA elements, non-linearities are allowed in the dynamic MPM analysis. For example, a non-linear traction law could be implemented by letting  $D_n$  and  $D_t$  be a function of the current relative displacements. The simple non-linearity used here was a bilinear law where  $D_n$  was different for an opened interface under tension than for a closed interface under compression. Since MPM with contact methods [9, 6] already detects separation or contact (in tasks (ii) and (iv) above), the imperfect interface tasks used that information. When the interface is in contact, the compressive  $D_n$  was used; when the interface is separated, the tensile  $D_n$  was used.

Non-linearities associated with the state of the interface are more difficult to implement. For example, imagine modeling interfacial damage where the interface fails at some critical opening displacement. If the surfaces are separated but not yet failed, the interface tractions will be a function of the opening displacement. If the surfaces are separated but has failed, however, the tractions should be zero even if the opening displacement returns to a low value. In other words, the normal traction depends on relative displacement *and* on the failure state of the interface. The problem implementing such history-dependent interfaces in MPM is that the solution resides on the particles while the interface calculations are done on the nodes. Since the interfaces may translate through the grid during a calculation, interface state properties can not be on the nodes. A potential scheme would be to calculate evolution of damage on interfacial nodes and extrapolate that information back to the particles. On subsequent time steps, the particles could extrapolate the damage information to the possibly new interface nodes, which could use that information to calculate traction. Implementing such a scheme is a subject for future work.

A related interface state property is dealing with imperfect interfaces formed during an analysis. The calculation of relative surface displacements (see Eq. (38)) is based on extrapolated particle displacements. This equation implies that surfaces have zero relative displacement when the particles have zero displacement. In other words, this analysis assumes all imperfect interfaces are initially in contact with zero traction. Imagine two objects moving together during an analysis and forming a new imperfect interface. Dealing with that new imperfect interface would require methods to detect interface formation and to determine the subsequent displacement condition for surface contact with zero traction. All calculations in this paper were for initially-coincident interfaces. Most problems involving imperfect interfaces fall into this category.

As  $D_n$  and/or  $D_t$  approach infinity, an imperfect interface converges to a perfect interface. In static FEA, no problems arise when  $D_n$  or  $D_t$  are large. In dynamic MPM, however, increasing interface parameters can lead to overly stiff equations and numerical instabilities. The solution is to handle perfect interfaces as a special case. Imagine the normal and tangential directions to be either imperfect (with specified  $D_n$  or  $D_t$  values) or perfect. Imperfect directions proceed as above for an imperfect interface. Perfect directions use stick contact conditions [9, 6].

Furthermore, since a perfect interface is not a contact surface, it uses stick conditions regardless of whether the interface is separated or in contact.

### 3. Results and Discussion

This section compares static and dynamic numerical analyses to analytical solutions. Since there are few analytical solutions with imperfect interfaces, two new analytical models were derived.

#### 3.1. Double Lap Shear Specimen

Figure 4 shows a double lap shear (DLS) specimen commonly used to characterize interfacial failure. The failure load defines interfacial strength, but the initial compliance depends on interface quality. As derived in the appendix using shear lag analysis, for the special case in which all three layers have the same thickness,  $t$ , and mechanical properties, the compliance of the bonded region of the specimen is

$$\frac{C}{C_\infty} = 1 + \frac{\tanh \frac{l\beta}{2} + 9 \tanh \frac{l\beta}{4}}{4l\beta} + \frac{3E_{yy}t\beta}{4lD_t} \operatorname{csch} \frac{l\beta}{2} \quad (40)$$

This equation has been simplified and corrected from published paper; calculations in paper are correct)

where  $C_\infty = l/(3tWE_{yy})$  is the compliance of an infinitely long bond line,  $E_{yy}$  is the axial modulus of the strips,  $W$  is specimen width,  $l$  is the length of the bond line, and  $\beta$  is the optimal shear-lag parameter [13], which for identical strips simplifies to

$$\beta = \sqrt{\frac{6G_{xy}}{t^2E_{yy} \left(1 + \frac{2G_{xy}}{tD_t}\right)}} \quad (41)$$

where  $G_{xy}$  is the  $x$ - $y$  plane shear modulus of the strips. Finally, accounting for specimen arm length  $L$ , the complete specimen stiffness is

$$k = \frac{1}{C + \frac{3L}{2tWE_{yy}}} \quad (42)$$

Calculations were run for DLS specimens made from wood strands used for oriented strand boards (OSB). Such strands are cut from logs using a strander [1]. The long axis of a strand is predominantly in the wood grain direction and thus  $E_{yy} = E_L \approx 10$  GPa where  $L$  is the longitudinal direction of wood and the value is a typical longitudinal modulus for wood [14]. The stranding process produces a mixture of radial ( $R$ ) and tangential ( $T$ ) directions in the thickness direction or strands; thus  $G_{xy}$  was set to an average of typical  $G_{LR}$  and  $G_{LT}$  for wood or about 0.5 GPa. The shear lag analysis requires only these properties. The FEA and MPM analyses needed additional values for  $E_{xx} = 1$  GPa (transverse modulus of wood) and  $\nu_{xy} = 0.2$  (from  $\nu_{LR}$  and  $\nu_{LT}$  of wood). Typical strand thicknesses are 0.6 mm. The specimen dimensions were  $t = 0.6$  mm,  $l = 25$  mm,  $L = 5$  mm, and  $W = 10$  mm.

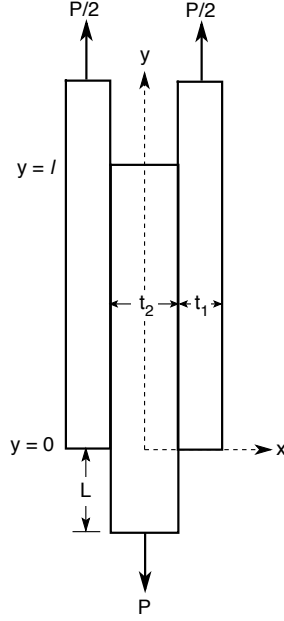


Figure 4: A symmetric double lap shear specimen with strands of thickness  $t_1$  and  $t_2$ , bond lines of length  $l$ , and ends tabs of length  $L$ . The specimen width is  $W$ .

Because shear dominates the interface effects in DLS specimens, the first calculations varied  $D_t$  from 2 MPa/mm to  $\infty$  while the normal direction was perfect ( $D_n = \infty$ ). The FEA calculations used 504 eight-node, quadrilateral elements. The interface had 24 six-node, interface elements. The MPM calculations used a square grid of  $0.1 \times 0.1$  mm elements with four particles per element for a total 10800 material points. In the dynamic MPM calculations, the load was ramped up over 0.5 msec and damping was used to converge to static results [15]. The results for specimen stiffness by FEA and MPM are plotted in Fig. 5 along with predictions by shear lag analysis. All results agreed validating both the imperfect interfaces in FEA and MPM and the new shear lag analysis for a DLS specimen.

Stiffness can be found from FEA results by two methods. A displacement method finds the stiffness from

$$k = \frac{P}{\langle \Delta_{top} \rangle - \langle \Delta_{bottom} \rangle} \quad (43)$$

where  $\langle \Delta_{top} \rangle$  and  $\langle \Delta_{bottom} \rangle$  are average  $y$ -direction displacement on the top and bottom of the specimen. Alternatively, because the interface elements are based on rigorous variational mechanics [3], the stiffness can be found by energy methods. Integrating the boundary of the specimen, the total energy is

$$U = \int_{\Gamma} \frac{1}{2} \vec{T} \cdot \vec{u} dS = \frac{1}{2} P \left( \langle \Delta_{top} \rangle - \langle \Delta_{bottom} \rangle \right) \quad (44)$$

leading to

$$k = \frac{P^2}{2U} \quad (45)$$

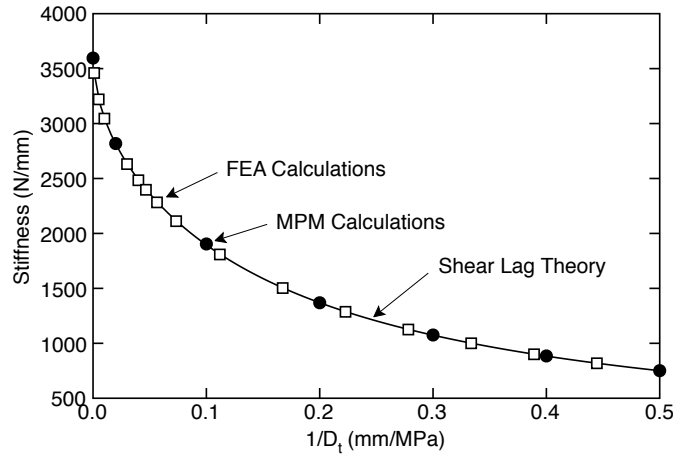


Figure 5: The stiffness of a double lap shear specimen as a function of the tangential interface parameter,  $D_t$ , calculated by FEA, MPM, or shear lag theory.

These two approaches gave identical results showing that the elements correctly included energetics of imperfect interfaces. The energy method is usually easier because it simply sums energy in all elements. The displacement method requires locating and analyzing all nodal displacements on the ends of the specimen. The current MPM implementation included no interfacial energy calculations and therefore stiffness was found by the displacement method.

The interfacial normal stresses in the numerical results had both tension and compression. Although the shear lag analysis does not handle normal direction effects, those effects can be studied numerically. Figure 6 shows three FEA results with different interface properties in the normal direction. The FEA curve labeled “ $D_n = \infty$ ” repeats the results from Fig. 5 (drawn as a solid line instead of symbols). The FEA curve labeled “ $D_n = 1$ ” is for  $D_n = 1$  MPa/mm; it shows a slight drop in specimen stiffness. The normal interface stiffness had very little effect unless it was very low and the shear stiffness was very high ( $D_t > 50$  MPa/mm). Figure 7 shows the interfacial normal displacement discontinuity along the interface. The FEA results when  $D_n = 1$  MPa/mm (dashed line) had negative displacements indicating the two surfaces interpenetrated. This behavior may be acceptable if the interface is modeling a finite dimension interphase, but otherwise interpenetration should be prevented. Since the FEA approach is linear, it can not have different stiffnesses in compression and tension, but one can assign different stiffnesses to different parts of the interface. The FEA curve labeled “ $D_n = 1$  ( $y < 12.5$ ) or  $\infty$  ( $y > 12.5$ )” is for a two-zone calculation where the normal direction had  $D_n = 1$  MPa/mm for the lower half of the specimen, but  $D_n = \infty$  for the top half. The two-zone model slightly increased the stiffness (see Fig. 6). It prevented interpenetration in the top half of the specimen, but some still remained in the bottom half (see dotted curve in Fig. 7).

In principle, an iterative FEA procedure could prevent interpenetration by setting  $D_n = \infty$  where ever there is contact. An alternative approach is to use a non-linear method with a perfect interface in compression but a finite  $D_n$  in tension. The MPM method can handle such nonlinear calculations and the results are shown in Figs. 6 and 7. The MPM points labeled “ $D_n = \infty$ ” repeats the results from Fig. 6 and adds some points. The MPM points labeled “ $D_n =$

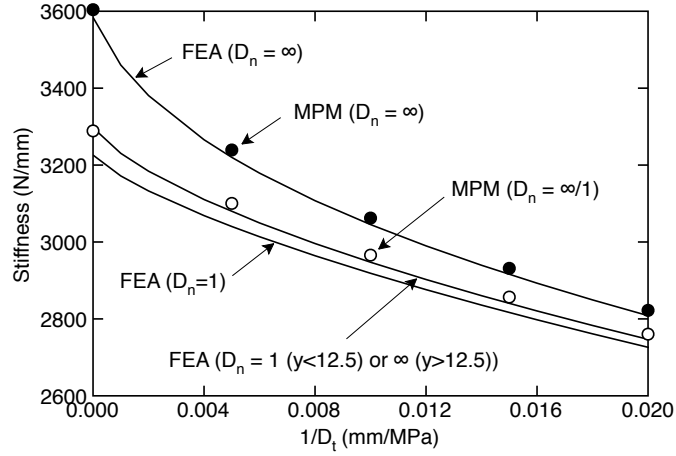


Figure 6: The effect of the normal interface parameter,  $D_n$ , on the stiffness of a double lap shear specimen as a function of the tangential interface parameter,  $D_t$ . The FEA results (lines) are for a perfect normal interface ( $D_n = \infty$ ), a linear imperfect normal interface ( $D_n = 1$ ), and a specimen with perfect normal interface on top, but an imperfect one on the bottom ( $D_n = 1$  ( $y < 12.5$ ) or  $\infty$  ( $y > 12.5$ )). The MPM results are for a linear imperfect normal interface ( $D_n = 1$ ) or a bilinear normal interface perfect in compression but imperfect in tension ( $D_n = \infty/1$ ).

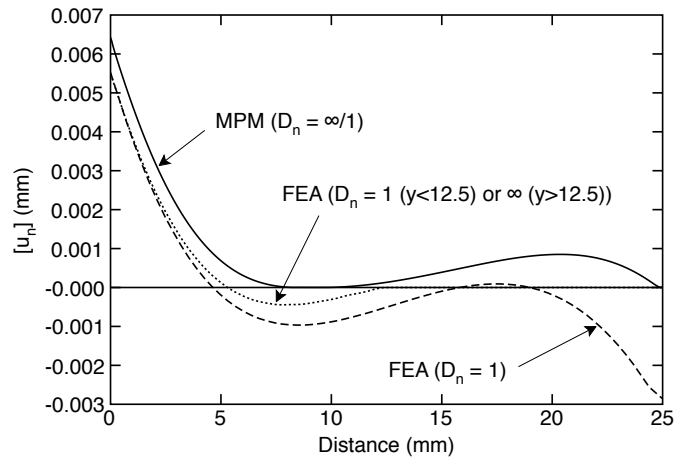


Figure 7: The displacement discontinuity in the normal direction across the interface in a double lap shear specimen. The FEA results (lines) are for a linear imperfect normal interface ( $D_n = 1$ ), and a specimen with perfect normal interface on top, but an imperfect one on the bottom ( $D_n = 1$  ( $y < 12.5$ ) or  $\infty$  ( $y > 12.5$ )). The MPM results are for a bilinear normal interface perfect in compression but imperfect in tension ( $D_n = \infty/1$ ).

$\infty/1$ ” are for calculations with a perfect interface in compression, but with  $D_n = 1$  MPa/mm in tension. The specimen stiffness decreased compared to  $D_n = \infty$  and was close to the two-zone FEA results. Figure 7 shows that the MPM results correctly prevented interpenetration and reveals an additional opening region in the top half of the specimens. The MPM results correctly modeled the non-linear interface. The two-zone FEA results only approximated the effects of the non-linearity; it was a good approximation because the stiffness was close to the MPM results.

### 3.2. Double Cantilever Beam Specimen

Figure 8 shows a double cantilever beam (DCB) specimen commonly used to characterize adhesive fracture. In the illustrated loading of a symmetric specimen, there are no shear displacements along the bond line. The effect of imperfect interface on the initial stiffness is thus due only to normal displacement discontinuities. As derived in the appendix using the beam-on-elastic-foundation model [16, 17, 18], the load-point compliance of a DCB specimen is

$$\frac{C}{C_0} = 1 + 3\frac{\Delta}{a} + 3\left(\frac{\Delta}{a}\right)^2 + \frac{3}{2}\left(\frac{\Delta}{a}\right)^3 \quad (46)$$

where  $C_0 = 8a^3/(WE_{xx}h^3)$  is the compliance of a DCB specimen by simple beam theory,  $a$  is crack length,  $E_{xx}$  is the axial modulus of the strips,  $W$  is specimen width,  $h$  is the depth of each arm, and  $\Delta$  is

$$\Delta^4 = \frac{WE_{xx}h^3}{3} \left( \frac{1}{2WD_n} + \frac{1}{k_b} \right) \quad (47)$$

where  $D_n$  is the normal interface parameter and  $k_b$  is a foundation stiffness accounting for shear deformation and crack-root rotation [17, 19]. In other words, even if the interface is perfect ( $D_n \rightarrow \infty$ ), the compliance of a DCB specimen is larger than  $C_0$  due to shear effects; those effects are modeled by a finite value for  $k_b$ .

Calculations were run for DCB specimens with wood strands and the grain direction in the  $x$  direction. The wood properties were the same as used for the DLS specimen. The arm thickness and width were  $t = 0.6$  mm and  $W = 10$  mm. The total length was 50 mm with the crack in the middle or  $a = 25$  mm. The FEA calculations used 250 eight-node, quadrilateral elements. The interface had 10 six-node, interface elements. The MPM calculations used a square grid of  $0.1 \times 0.1$  mm elements with four particles per element for a total 24000 material points. In the dynamic MPM calculations, the load was ramped up over 1 msec and damping was used to converge to static results [15]. Specimen stiffness calculated by FEA or MPM is plotted in Fig. 9 along with the beam-on-elastic-foundation model. The theoretical calculations required a value for  $k_b$ . This value was found by FEA analysis with a perfect interface to be  $k_b = 7808$  MPa. All results agreed well although MPM results were slightly lower than FEA results and the theory. Note that  $D_n$  had a small effect on stiffness.  $D_n$  had to be less than 1 MPa to significantly alter the specimen stiffness. Furthermore, since  $D_n \ll k_b/(2W) = 390.4$  MPa/mm (except for a perfect interface with  $1/D_n = 0$ ), the effect of  $k_b$  on the imperfect interface results was negligible. The FEA results gave identical stiffness by either a displacement method (Eq. (43)) or an energy method (Eq. (45)).

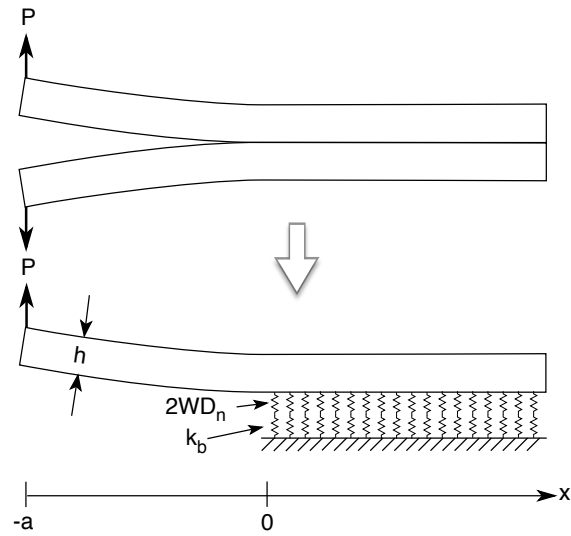


Figure 8: A double cantilever beam specimen with crack length  $a$  and arms of thickness  $h$ . The specimen width is  $W$ . The bottom shows a beam-on-elastic-foundation model for the specimen.

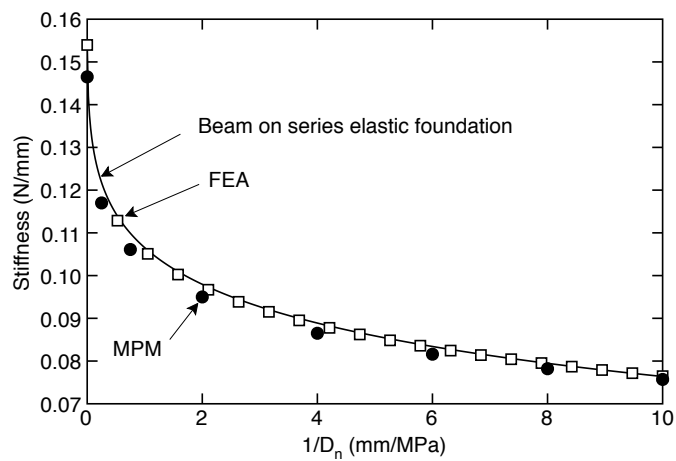


Figure 9: The stiffness of a double cantilever beam specimen as a function of the normal interface parameter,  $D_n$ , calculated by FEA, MPM, or beam-on-elastic-foundation theory.

### 3.3. Imperfect Interface Wave Transmission and Reflection

Imperfect interfaces are used to model wave transmission across an interface or through a material with cracks and interfaces [5, 20, 21]. For a plane wave incident normally on a straight imperfect interface with linear traction law, the fraction of the wave energy transmitted through the interface was derived to be [20, 21]:

$$T = \frac{D_n^2}{D_n^2 + \pi^2 f^2 \rho^2 v^2} \quad (48)$$

where  $f$  is wave frequency,  $\rho$  is density, and  $v = \sqrt{E/\rho}$  is the tensile wave speed.

Dynamic MPM calculations were run for wave transmission through a  $150 \times 100 \times 1$  mm block with an imperfect interface located at  $x = 50$  mm. Because the theory assumes isotropic materials, the calculations used an isotropic material with  $E = 410$  GPa,  $\nu = 0.28$ ,  $\rho = 15$  g/cm<sup>3</sup>, and  $v = 5235$  m/sec. A displacement impulse defined by

$$x(t) = \frac{x_0}{2}(1 - \cos 2\pi f t) \quad \text{for } 0 \leq t \leq \frac{1}{2f} \quad (49)$$

was applied to the specimen's left edge at  $x = 0$ . This impulse induces a single tensile stress pulse if  $x_0 < 0$  or a single compressive stress pulse if  $x_0 > 0$ . The energy of the transmitted pulse was calculated from the square of ratio of the amplitudes of the transmitted stress to the incident stress. A comparison of MPM results for either a tensile or compressive pulse (with  $f = 100$  kHz) and for either a linear imperfect interface (as a function of  $D_n$ ) or a non-linear imperfect interface (with specified  $D_n$  for tensile stress but  $D_n = \infty$  for compressive stress) to theoretical predictions is given in Fig. 10. Linear interface results (labeled "L") agreed well with the theory. For a non-linear interface (labeled "NL"), a tensile pulse was identical to the linear interface results because the stresses were always tensile. For a compressive pulse, however, the non-linear interface was always perfect and thus 100% of the energy was transmitted.

Transmission energy calculations assumed the shape of the transmitted pulse is identical to the shape of the incident pulse. Figure 11 shows calculated incident, transmitted, and reflected pulses for a tensile wave with about 50% energy transmitted. The transmitted pulse had a similar shape, but some slight deviations. The shape of the reflected pulse was complex and became both tensile and compressive. This pulse shape differs significantly from reflection at a perfect interface, where the reflected wave is unaltered in shape (although it may or may not invert depending on the relative properties of the two materials), at a rigid interface, where the pulse inverts in shape, or at a free surface, where the pulse is reflected with unaltered shape [22]. A concern with cohesive elements, particularly when cohesive elements with arbitrary initial stiffness must be located throughout the mesh, is that they will introduce spurious wave speeds [23]. Figure 11 shows that initial stiffness can affect wave speeds; cohesive elements should select initial stiffness for 100% energy transmission to avoid artifacts. For imperfect interfaces, the changes in pulse shapes are modeling real effects of wave reflection at the interface. Some preliminary analytical calculations showed the reflected wave pulse found by MPM was the expected wave pulse for an imperfect interface [24], *i.e.*, the effects are real and not spurious. The shape of wave reflections from an imperfect interfaces has received little attention.

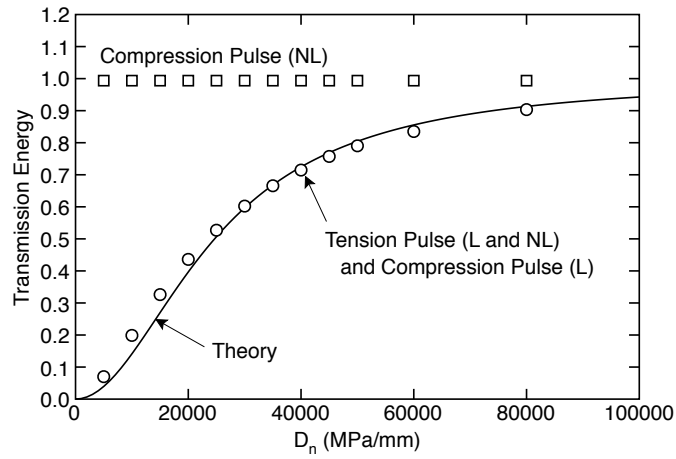


Figure 10: Transmission energy across an imperfect interface as calculated by MPM or theory. The MPM results are for either a tensile stress pulse or a compressive stress pulse.

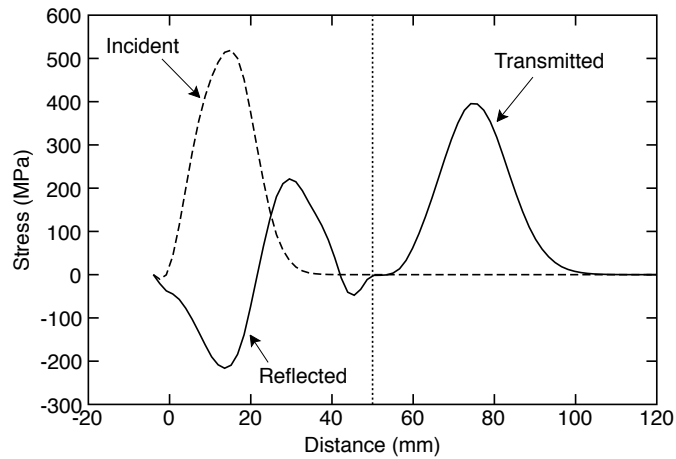


Figure 11: Shapes of the incident prior to reaching the interface (dashed line), and the transmitted and reflected pulses after passing the interface (solid lines) as calculated by MPM. The interface is located at the dotted line at 50 mm.

### 3.4. Experimental Determination of Interface Parameters

The FEA and MPM methods can incorporate imperfect interfaces into models of composite materials and parametrically assess the role of the interface on composite properties. Interface calculations are only of practical use when combined with experimental methods for determining the interface parameters. All examples were selected to validate the numerical imperfect interfaces, but they were also selected as potential candidates for experimental work on interfaces. This section discusses some possibilities and limitations.

The stiffness of a DLS specimen is significantly affected by  $D_t$  suggesting its stiffness could be used to determine tangential interfacial properties. The main limitation is that shear effects and therefore  $D_t$  effects are end effects. Taking the limit as the specimen becomes long reveals the end-effect nature of stress transfer:

$$\lim_{l \rightarrow \infty} \frac{C}{C_\infty} = 1 \quad \text{or} \quad \lim_{l \rightarrow \infty} k = \frac{3tWE_{yy}}{l} \quad (50)$$

In other words, as  $l$  gets long the specimen approaches a simple tensile bar with no interface. The lap geometry on the ends gets tensile load into the specimen, but end effects become negligible as the specimen gets long. The solution is to select a specimen sufficiently short that end effects play a role in specimen stiffness. A dimensionless number characterizing the magnitude of end effects is  $\beta l$  which maximizes for a perfect interface. For identical strands, the maximum characteristic number is

$$\beta l = \frac{l}{t} \sqrt{\frac{6G_{xy}}{E_{yy}}} \quad (51)$$

For the wood specimens analyzed above,  $\beta l = 22.8$ . Smaller values of  $\beta l$  are better, which for given mechanical properties can be achieved by selecting shorter or thicker strands. Larger values of  $\beta l$  would reduce the accuracy of determining  $D_t$ .

The DCB specimen was selected for potentially determining  $D_n$ . Unfortunately, calculations showed that  $D_n$  does not significantly affect the load-point stiffness of a DCB specimen unless it is very low. In contrast,  $D_n$  strongly affected wave transmission. Furthermore, the experiment could be tailored for optimal determination for any range of  $D_n$  values by tuning the frequency to the expected  $D_n$  such that  $D_n \approx \pi f \rho v$ . Although wave transmission through an imperfect interface between perfectly homogeneous and isotropic bodies works well in theory, there may be experimental difficulties in practice. In wood, interface effects may be hard to distinguish from other effects on wave transmission through a heterogeneous, anisotropic, and cellular material.

### 3.5. Stiff Interphases

Most work on imperfect interfaces has allowed interface parameters to vary from 0, for a debonded interface, to infinity, for a perfect interface [5]. This approach makes sense for a real 2D interface, but for 2D model of a 3D interphase, perhaps a wider range in interface parameters is possible. For a linear-elastic interphase of thickness  $t_i$ , a simple series analysis

for either tensile or shear loading (to left side of Fig. 1) such that the total deformation of the full model agrees with the total deformation of the interface model on the right of Fig. 1 leads to

$$\frac{1}{D_n} = t_i \left[ \frac{1}{E_i} - \frac{1}{2} \left( \frac{1}{E_1} + \frac{1}{E_2} \right) \right] \quad \text{and} \quad \frac{1}{D_t} = t_i \left[ \frac{1}{G_i} - \frac{1}{2} \left( \frac{1}{G_1} + \frac{1}{G_2} \right) \right] \quad (52)$$

where  $E_i$ ,  $E_1$ ,  $E_2$ ,  $G_i$ ,  $G_1$ , and  $G_2$  are the tensile and shear moduli of the interface and the two substrates, respectively. Taking the interphase moduli as spanning from debonded ( $E_i, G_i \rightarrow 0$ ) to rigid ( $E_i, G_i \rightarrow \infty$ ), the interface parameters would span from 0 ( $1/D_n = 1/D_t = \infty$ ) for a debonded interphase to a negative value (e.g.,  $1/D_n \rightarrow -(t_i/2)((1/E_1) + (1/E_2))$ ) for a rigid interphase. For an actual 2D interface ( $t_i = 0$ ), this view reduces to the prior view of interface parameters between zero and infinity. For a 3D interphase, extending interface parameters into negative values may allow modeling of stiffer interphases. For example, glue penetration into the wood cells of a glue line may reinforce the wood near the bond creating a stiffened interphase region. The possible negative values are limited by the rigid interphase limit. The negative energies associated with a stiffer interphase (see Eq. (4)) are reconciled by equating them with a *reduction* in energy rather than a negative energy.

## Acknowledgements

This work was supported by a grant from the United States Department of Agriculture, Cooperative State Research, Education, and Extension Service, National Research Initiative, Contract No. 2006-35504-17444 and by the University of Utah Center for the Simulation of Accidental Fires and Explosions (C-SAFE), funded by the Department of Energy, Lawrence Livermore National Laboratory, under Subcontract B341493.

## Appendix A. Double Lap Shear Specimen Analysis

A generalized shear lag method [25, 13] was used to derive an analytical result for stiffness of the double lap shear (DLS) specimen in Fig. 4 including the effects of an imperfect interface. Due to symmetry, only half the specimen, which is a two layer problem, was analyzed. The shear lag equation is [25, 13]

$$\frac{d^2 \langle \sigma_{yy}^{(1)} \rangle}{dy^2} - \beta^2 \langle \sigma_{yy}^{(1)} \rangle = -\beta^2 \sigma_{yy}^{(\infty)} \quad (A.1)$$

The general solution for the average axial stress in layer 1 is

$$\langle \sigma_{yy}^{(1)} \rangle = \sigma_{yy}^{(\infty)} + ae^{\beta y} + be^{-\beta y} \quad (A.2)$$

where

$$\sigma_{yy}^{(\infty)} = \frac{2E_{yy}^{(1)}}{(2t_1 E_{yy}^{(1)} + t_2 E_{yy}^{(2)})} \frac{P}{(2t_1 + t_2)W} \quad (A.3)$$

is the far-field stress in layer 1 (*i.e.*, the stress far from the ends in an infinitely long specimen) and  $E_{yy}^{(i)}$  is the  $y$ -direction modulus of layer  $i$ . The optimal shear lag parameter,  $\beta$ , is [13]:

$$\beta = \sqrt{\frac{\frac{1}{t_1 E_{yy}^{(1)}} + \frac{2}{t_2 E_{yy}^{(2)}}}{\frac{t_1}{3G_{xy}^{(1)}} + \frac{t_2}{6G_{xy}^{(2)}} + \frac{1}{D_t}}} \quad (\text{A.4})$$

where  $G_{xy}^{(i)}$  is the  $x$ - $y$  plane shear modulus of layer  $i$  and  $D_t$  is the tangential interfacial parameter for the interface between layers 1 and 2. The constants  $a$  and  $b$  are determined using the boundary conditions on layer 1 of

$$\langle \sigma_{yy}^{(1)}(l) \rangle = \sigma_0^{(1)} = \frac{P}{2t_1 W} \quad \text{and} \quad \langle \sigma_{yy}^{(1)}(0) \rangle = 0 \quad (\text{A.5})$$

leading to

$$a = -\frac{\sigma_0^{(1)} e^{\beta l} + \sigma_{yy}^{(\infty)} (1 - e^{\beta l})}{1 - e^{2\beta l}} \quad \text{and} \quad b = \frac{\sigma_0^{(1)} e^{\beta l} - \sigma_{yy}^{(\infty)} e^{\beta l} (1 - e^{\beta l})}{1 - e^{2\beta l}} \quad (\text{A.6})$$

By force balance, the average stress in layer 2 is

$$\langle \sigma_{yy}^{(2)} \rangle = \frac{P - 2t_1 W \langle \sigma_{yy}^{(1)}(l) \rangle}{t_2 W} \quad (\text{A.7})$$

Finally, the interfacial shear stress is [25]:

$$\tau_{xy} = -t_1 \frac{d \langle \sigma_{yy}^{(1)} \rangle}{dy} = -t_1 \beta (a e^{\beta y} - b e^{-\beta y}) \quad (\text{A.8})$$

The compliance of the specimen between points at  $y = 0$  and  $y = l$  is  $C = \Delta u / P$  where  $\Delta u$  is the deformation between those points. The deformations are found by integrating the average axial strains and accounting for interfacial slip:

$$\Delta u = \int_0^{l/2} \frac{\sigma_{yy}^{(2)}}{E_{yy}^{(2)}} dy + \int_{l/2}^l \frac{\sigma_{yy}^{(1)}}{E_{yy}^{(2)}} dy + \frac{\tau_{xy}(l/2)}{D_t} \quad (\text{A.9})$$

The first two terms are displacement across the bottom half of layer 2 and the top half of layer 1, respectively. The last term is interfacial slip at the midpoint of the specimen. These displacements are easily evaluated using the stress state derived above. The shear stress at the midpoint simplifies to

$$\tau_{xy}(l/2) = \frac{t_1 \beta \sigma_0^{(1)} e^{\beta l/2}}{1 - e^{\beta l}} \quad (\text{A.10})$$

The compliance calculation is straight forward, but leads to a lengthy equation. The calculations in this paper were all for identical strips or the special case where  $t_1 = t_2 = t$ ,  $E_{yy}^{(1)} = E_{yy}^{(2)} = E_{yy}$  and  $G_{xy}^{(1)} = G_{xy}^{(2)} = G_{xy}$ . The compliance for this special case is given in the text of the paper in Eq. (40).

## Appendix B. Double Cantilever Beam Specimen Analysis

Using the beam-on-elastic-foundation model [16, 17], the equation for the upper-arm deflection,  $v(x)$ , in the bonded region is

$$\frac{d^4v(x)}{dx^4} = -\frac{k_1}{E_{xx}I}v(x) \quad (\text{B.1})$$

where  $E_{xx}$  is the x-direction modulus of the arms,  $I = Wh^3/12$  is the second moment of inertia, and  $k_1$  is the stiffness of the elastic foundation. Here the elastic foundation is modeled as two springs in series. One spring reflects the imperfect interface (with stiffness  $2WD_n$ ) and the second spring is the *effective* stiffness to the lower arm ( $k_b$ ) [17, 18]:

$$\frac{1}{k_1} = \frac{1}{2WD_n} + \frac{1}{k_b} \quad (\text{B.2})$$

From Ref. [18], the displacement in the bonded region is

$$v(x) = \frac{P\Delta^2}{2E_{xx}I} \left[ (a + \Delta) \cos \frac{x}{\Delta} - a \sin \frac{x}{\Delta} \right] e^{-x/\Delta} \quad \text{for } x \geq 0 \quad (\text{B.3})$$

where  $\Delta$  is defined in Eq. (47). At the crack tip ( $x = 0$ ) the displacement and slope are

$$v(0) = \frac{P\Delta^2(a + \Delta)}{2E_{xx}I} \quad \text{and} \quad v'(0) = -\frac{P\Delta(2a + \Delta)}{2E_{xx}I} \quad (\text{B.4})$$

To the left of the crack tip in the the free-arm section, the beam equation is

$$\frac{d^2v(x)}{dx^2} = \frac{P(a + x)}{EI} \quad (\text{B.5})$$

Integrating twice and finding the constants by requiring continuity in  $v(x)$  at  $x = 0$  leads to

$$v(x) = \frac{P}{6EI} (x^3 + 3a(x - \Delta)^2 - 3x\Delta^2 + 3\Delta^3) \quad \text{for } x \leq 0 \quad (\text{B.6})$$

Finding the total displacement at the ends of the arms ( $2v(-a)$ ), the load-point compliance is given by Eq. (46).

## References

- [1] J. G. Haygreen, J. L. Bowyer, Forest Products and Wood Science: An Introduction, Iowa State University Press, Ames, Iowa, USA, 1996.
- [2] Z. Hashin, Thermoelastic properties of fiber composites with imperfect interface, Mech. of Materials 8 (1990) 333–348.
- [3] Z. Hashin, Extremum principles for elastic heterogenous media with imperfect interfaces and their application to bounding of effective moduli, Journal of the Mechanics and Physics of Solids 40 (4) (1992) 767–781.

- [4] Z. Hashin, Thermoelastic properties of particulate composites with imperfect interface, *Journal of the Mechanics and Physics of Solids* 39 (6) (1991) 745–762.
- [5] P. A. Martin, Boundary integral equations for the scattering of elastic waves by elastic inclusions with thin interface layers, *Journal of Nondestructive Evaluation* 11 (3/4) (1992) 167–174.
- [6] S. G. Bardenhagen, J. E. Guilkey, K. M. Roessig, J. U. Brackbill, W. M. Witzel, J. C. Foster, An improved contact algorithm for the material point method and application to stress propagation in granular material, *Computer Modeling in Engineering & Sciences* 2 (2001) 509–522.
- [7] A. Needleman, A continuum model for void nucleation by inclusion debonding, *J. Appl. Mech.* 54 (1987) 525–531.
- [8] D. Sulsky, Z. Chen, H. L. Schreyer, A particle method for history-dependent materials, *Comput. Methods Appl. Mech. Engrg.* 118 (1994) 179–186.
- [9] S. G. Bardenhagen, J. U. Brackbill, D. Sulsky, The material point method for granular materials, *Computer Methods in Applied Mechanics and Engineering* 187 (2000) 529–541.
- [10] J. A. Nairn, Material point method calculations with explicit cracks, *Computer Modeling in Engineering & Sciences* 4 (2003) 649–664.
- [11] J. A. Nairn, On the calculation of energy release rates for cracked laminates with residual stresses, *Int. J. Fract. Mech.* 139 (267–293).
- [12] Y. Guo, J. A. Nairn, Three-dimensional dynamic fracture analysis in the material point method, in preparation (2006).
- [13] J. A. Nairn, Generalized shear-lag analysis including imperfect interfaces, in press (2005).
- [14] J. Bodig, B. A. Jayne, *Mechanics of Wood and Wood Composites*, Van Nostran-Reinhold Co, Inc., New York, 1982.
- [15] G. Ayton, A. M. Smondyrev, S. G. Bardenhagen, P. McMurtry, G. A. Voth, Interfacing molecular dynamics and macro-scale simulations for lipid bilayer vesicles, *Biophys J* 83 (2002) 1026–1038.
- [16] M. F. Kanninen, An augmented double cantilever beam model for studying crack propagation and arrest, *Int. J. Fract.* 9 (1973) 83–92.
- [17] J. G. Williams, End corrections for orthotropic dcb specimens, *Comp. Sci. & Tech.* 35 (1989) 367–376.
- [18] J. G. Williams, Analytical solutions for cohesive zone models, *J. Mech. Phys. Solids* 50 (2002) 809–825.
- [19] S. Hashemi, A. J. Kinloch, J. G. Williams, The analysis of interlaminar fracture in uniaxial fibre reinforced polymer composites, *Proc. R. Soc. Lond. A347* (1990) 173–199.
- [20] R. B. Thompson, C. J. Fiedler, The effects of crack closure on ultrasonic scattering measurements, in: D. O. Thompson, D. E. Chimenti (Eds.), *Review of Progress in Quantitative Nondestructive Evaluation 3A*, Plenum Press, New York, 1984, pp. 207–215.
- [21] Y. C. Angel, J. D. Achenbach, Reflection and transmission of elastic waves by a periodic array of cracks, *J. Appl. Mech.* 52 (1985) 33–41.
- [22] A. Bedford, D. S. Drumheller, *Elastic Wave Propagation*, John Wiley & Sons, New York, 1994.
- [23] R. de Borst, J. J. C. Remmers, A. Needleman, Mesh-independent discrete numerical representations of cohesive zone models, *Eng. Fract. Mech.* 73 (2006) 160–177.
- [24] P. A. Martin, Personal communication (2006).
- [25] J. A. Nairn, D.-A. Mendels, On the use of planar shear-lag methods for stress-transfer analysis of multilayered composites, *Mechanics of Materials* 33 (2001) 335–362.